Computational analysis of a thin airfoil with different surface roughness types

A project presented to
The Faculty of the Department of Aerospace Engineering
San Jose State University

in partial fulfillment of the requirements for the degree
Master of Science in Aerospace Engineering

by

Thiruvateeswaran Suresh

December 2024

Approved by

Dr. Yawo Ezunkpe
Faculty Advisor

Abstract

Computational analysis of a thin airfoil with different surface roughness types
Thiruvateeswaran Suresh

This project aims to investigate the aerodynamic and thermal characteristics of an irregular surface of a highspeed wing by simplifying its shape to that of a thin flat plate. The research will involve analyzing this flat plate with different surface configurations. Various computational software tools will be employed throughout the project. First, SolidWorks will be used to design the geometry of the model. The definition of the mesh and the analysis will be done by Star CCM+ and ANSYS. These tools will be used to analyze the flat plate's aerodynamic and thermal properties. In addition to using commercial CFD software, the project will include the development of a custom solver to investigate the same aerodynamic and thermal problems. This self-developed solver will be compared with the results obtained from the commercial software to evaluate its accuracy and effectiveness. This project combines both simulation and custom solver development to gain a comprehensive understanding of the aerodynamic and thermal behaviors of an irregular supersonic wing as a flat plate.

Acknowledgments

I would like to acknowledge my family for giving me the support and foundation to focus on my education and pursue my dreams, and my success is due in part to their love and patience. I would also like to acknowledge my professor Dr. Yawo Ezunkpe who has encouraged, guided, and given me the skills I needed to grow professionally. Thank you all for your support.

Table of Contents

Abstract i
Acknowledgments ii
List of Figures iv
List of Tables vi
Nomenclature vii
1 Introduction 1
1.1 Motivation 1
1.2 Literature Survey 1
1.2.1 Surface roughness 1
1.2.2 Skin friction and temperature 1
1.2.3 Comparison of Models 2
1.2.4 Roughness Elements 3
1.3 Project Objective 5
1.4 Methodology 5
2 Geometric Design 6
2.1 Roughness Elements 6
2.1.1 Surface Topology 6
3 Theoretical Analysis of the Flow Field 7
3.1 Non-Dimensional Analysis 8
4 Grid generation and Boundary Conditions 12
4.1 Boundary Conditions 13
5 Results and Discussion 14
6 Conclusion 25
References 26
Appendix A: Solver Settings 28

List of Figures

Figure 1.1 Vortex behind the single roughness element 4
Figure 1.2 Streamwise vortices over roughness distributed at long distance 4
Figure 2.1 NACA 65206 airfoil 6
Figure 2.2 Roughness elements distribution 6
Figure 4.1 Unstructured triangular mesh 11
Figure 4.2 C-Type Domain 11
Figure 4.3 Domain setup 12
Figure 5.1 Smooth surface Mach contour 14
Figure 5.2 Smooth surface pressure contour 14
Figure 5.3 Top roughness Mach contour 14
Figure 5.4 Top roughness pressure contour 14
Figure 5.5 Bottom roughness Mach contour 14
Figure 5.6 Bottom roughness pressure contour 14
Figure 5.7 Trailing edge roughness Mach contour 14
Figure 5.8 Trailing edge roughness pressure contour 14
Figure 5.9 LE_top roughness Mach contour 15
Figure 5.10 LE_top roughness pressure contour 15
Figure 5.11 TE_top roughness Mach contour 15
Figure 5.12 TE_top roughness pressure contour 15
Figure 5.13 Smooth surface Mach contour 16
Figure 5.14 Smooth surface pressure contour 16
Figure 5.15 Top roughness Mach contour 16
Figure 5.16 Top roughness pressure contour 16
Figure 5.17 Bottom roughness Mach contour 17
Figure 5.18 Bottom roughness pressure contour 17
Figure 5.19 Trailing edge roughness Mach contour 17
Figure 5.20 Trailing edge roughness pressure contour 17
Figure 5.21 LE_top roughness Mach contour 17
Figure 5.22 LE_top roughness pressure contour 17
Figure 5.23 TE_top roughness Mach contour 17
Figure 5.24 TE_top roughness pressure contour 17
Figure 5.25 Smooth surface Mach contour 19
Figure 5.26 Smooth surface pressure contour 19
Figure 5.27 Top roughness Mach contour 19
Figure 5.28 Top roughness pressure contour 19
Figure 5.29 Bottom roughness Mach contour 19
Figure 5.30 Bottom roughness pressure contour 19
Figure 5.31 Trailing edge roughness Mach contour 19
Figure 5.32 Trailing edge roughness pressure contour 19
Figure 5.33 LE_top roughness Mach contour 20
Figure 5.34 LE_top roughness pressure contour 20
Figure 5.35 TE_top roughness Mach contour 20
Figure 5.36 TE_top roughness pressure contour 20

Figure 5.37 Smooth surface Mach contour 21
Figure 5.38 Smooth surface pressure contour 21
Figure 5.39 Top roughness Mach contour 22
Figure 5.40 Top roughness pressure contour 22
Figure 5.41 Bottom roughness Mach contour 22
Figure 5.42 Bottom roughness pressure contour 22
Figure 5.43 Trailing edge roughness Mach contour 22
Figure 5.44 Trailing edge roughness pressure contour 22
Figure 5.45 LE_top roughness Mach contour 22
Figure 5.46 LE_top roughness pressure contour 22
Figure 5.47 TE_top roughness Mach contour 23
Figure 5.48 TE_top roughness pressure contour 23

List of Tables

Table 1.1 Numerical roughness Data 2
Table 1.2 Boundary value measurements:
Summary of experimental conditions;
Summary of boundary layer values at x =0.56m 3
Table 4.1 Boundary Conditions 12
Table 4.2 Mesh Independence Study 12
Table 5.1 Data analysis of aerodynamic parameter for 0º angle of attack 13
Table 5.2 Data analysis of aerodynamic parameter for 3º angle of attack 15
Table 5.3 Data analysis of aerodynamic parameter for 6º angle of attack 18
Table 5.4 Data analysis of aerodynamic parameter for 9º angle of attack 20

Nomenclature

Symbols	Definition
α	Angle of attack
ρ	Density
L	Chord Length
μ	Dynamic viscosity
k	Thermal conductivity
k_s	Equivalent roughness height
C_f	Skin friction coefficient
Θ	Ratio of grid size/momentum thickness
δ	Boundary layer thickness
γ	Specific heat ratio
M	Mach number
Re	Reynolds number
Pr	Prandtl number
"X_∞"	Reference value/freestream value
∂	Partial derivative
e	Specific Internal energy
p	Pressure
T	Temperature
DNS	Direct Numerical Simulation
RANS	Reynolds Averaged Navier-Stokes

1 Introduction

1.1 Motivation

Understanding surface roughness is of much importance for the control and thermal management of high-speed vehicles. Research in low-speed incompressible flows is done in a wide range whereas when it comes to compressible high-speed flows, the study is very much limited [1]. So, understanding how the roughness will affect the flow transition and how the boundary layer is affected is key to improving the performance of the vehicle as most of the manufacturing process uses the method of additive manufacturing with 3D printing, which produces a rough finish rather than an expected smooth finish.
Supersonic airfoils are generally thin-shaped with sharp edges at the leading and trailing points of the airfoil. This is to prevent the formation of detached bow shock at the leading-edge part during its flow through supersonic speeds. The surface of this thin-shaped airfoil has a crucial impact on the performance of the airfoil due to its roughness value. The understanding of this surface boundary layer can be utilized for the optimization of the performance of the wing.

1.2 Literature Survey

1.2.1 Surface roughness

Due to the protrusions, the oblique shock structure and strength of the shock are influenced by all variables to varying extents. The shock location is altered by the height of the protrusion, the Reynolds number, and the shape of the protrusion, whereas the Mach number has only a slight influence [2]. Latin and Robert M obtained the full characterization of rough surface high-speed and high Reynolds number boundary layer, and the experiments demonstrated that the roughness height and the blockage of the rough-surfaced high-speed boundary layer flow has a huge impact on compressible turbulence terms whereas the kinematic turbulent quantities were less influenced [2]. The numerical data was almost identical to the experimental data in terms of increasing roughness height and blockage, skin friction, and friction velocity [2]. The flow structure angle increased as the surface roughness height increased, with the greatest influence occurring in the outer boundary layer region. [2].

1.2.2 Skin friction and temperature

Drag induced due to skin friction is important to calibrate accurately as it can result in errors in missile range calculations or lift generation calculations [3]. The differential equations are used to describe the 2-D flow by expressing the conservation of mass, momentum, and energy, defined in a boundary layer on a flat plate. These equations are called the Navier Stokes equation that Fan and Bowersox conducted the numerical analysis of high-speed flow over the rough surface, and they tested three algebraic models viz. Van Driest, Kragstad, and Cebeci-Chang for high-speed flow. From the examination, it was observed that when the roughness height increases, it tends to increase the thickness of the boundary layer due to additional turbulence and entrainment of freestream fluid [4].

The following table depicts the roughness data for each model used. With the information from Table 1.1, the conclusion of the integral properties of the smooth plate was made to be all within 5 percent of the experimental data.

Table 1.1 Numerical roughness data [4]

Model	δ (mm)	θ (mm)	C_f
Smooth	11.8	0.77	0.0015
2D, van Driest	16.8	1.23	0.0030
2D, Kragstad	19.0	1.41	0.0035
2D, Cebeci-Chang	18.6	1.37	0.0033
3D, van Driest	16.8	1.21	0.0029
3D, Kragstad	18.6	1.37	0.0034
3D, Cebeci-Chang	18.2	1.33	0.0032
80 Grit, van Driest	15.9	1.13	0.0027
80 Grit, Kragstad	16.8	1.21	0.0029
80 Grit, Cebeci-Chang	16.2	1.16	0.0028
36 Grit, van Driest	17.2	1.26	0.0031
36 Grit, Kragstad	19.3	1.45	0.0038
36 Grit, Cebeci-Chang	19.3	1.44	.0035
20 Grit, van Driest	17.2	1.29	0.0032
20 Grit, Kragstad	19.7	1.49	0.0040
20 Grit, Cebeci-Chang	20.5	1.53	0.0038

1.2.3 Comparison of models

Sharief et al discuss the efficiencies of two different solvers, which are k–omega, and stress–omega turbulence models, and are computed with the experimental data that is available for validation [5]. For smooth surfaces, both the models predicted more accurately the mean flow and turbulence quantities whereas the case for rough surfaces was different. For the rough surface, both models performed well for low roughness heights whereas for high roughness heights, it performed unsatisfactorily. The paper also concluded the k-omega model is better compared to the stress omega model. It was also found for the k-omega model, the boundary layer thickness maximized when the roughness height increased [5]. The following table depicts the roughness data for each model used.

Table 1.2 Boundary value measurements: (a) Summary of experimental conditions; (b) Summary of boundary layer values at x =0.56m [5]

Table 1
Summary of experimental conditions and some measured boundary layer values

Roughness condition	k_s (mm)	T_w (K)	M_∞	At measurement point $x = 0.56$ m			
				k_s^+	δ (mm)	θ (mm)	C_f
Smooth	0	276	2.75	0	12.4	0.80	0.0016
2D	1.09	274	2.73	289	16.8	1.32	0.0038
3D	0.91	273	2.73	241	15.8	1.29	0.0037
80 Grit	0.44	273	2.73	104	14.7	1.11	0.0030
36 Grit	1.42	273	2.72	395	18.0	1.43	0.0040
20 Grit	1.98	273	2.70	571	17.7	1.45	0.0041

Table 2
Summary of predicted boundary layer values at $x = 0.56$ m

Roughness condition	Turbulence model	δ (mm)	θ (mm)	C_f
Smooth	k–ω	10.77	0.75	0.00155
	Stress–ω	10.41	0.71	0.00145
2D	k–ω	15.47	1.18	0.00372
	Stress–ω	14.69	1.05	0.00346
3D	k–ω	15.17	1.09	0.00354
	Stress–ω	14.42	1.02	0.00338
80 Grit	k–ω	13.61	0.98	0.00293
	Stress–ω	13.47	0.96	0.00255
36 Grit	k–ω	16.01	1.31	0.00399
	Stress–ω	13.3	0.95	0.00352
20 Grit	k–ω	16.63	1.34	0.00441
	Stress–ω	13.08	0.93	0.00355

The stress omega model has no strong pros to overcome its computational cost. Overall, the k- omega model performed well than the stress omega model.

1.2.4 Roughness elements

Roughness elements can lead to premature laminar-turbulent transitions and higher heating at supersonic speeds. The intensity of vortices is proportionate to the size of roughness elements [6]. This roughness also generates a distribution of oblique shocks respective to the geometry of roughness elements [1]. The paper compares three different scenarios and compares the flow instabilities. fixed computations are performed by using the CFS3D Navier-Stokes code [7] which features high-order shock-capturing and is capable of computing discontinuities in the flow and accurate simulation of unsteady wave processes. In the first case, the roughness is distributed near the nose region of the blunt cone. In the second case, a single roughness element at a long distance from the nose is used. In this case, this element does not induce the laminar-turbulent transition when excited by the suction/blowing upstream at the considered flow parameters [7].

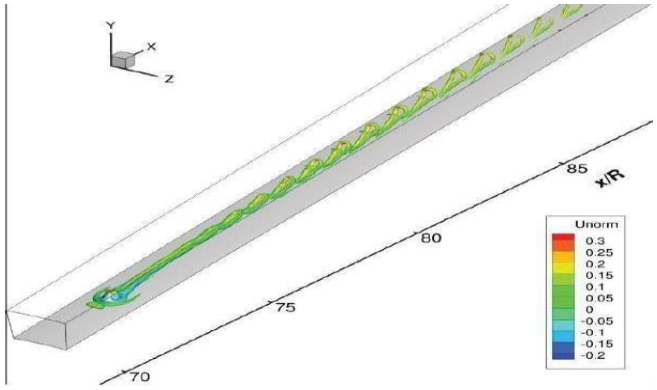

Figure 1.1 Vortex behind the single roughness element

In the third case, the roughness elements are distributed at long distances from the nose. This case forms a streamwise vortex disturbance with various characteristic scales.

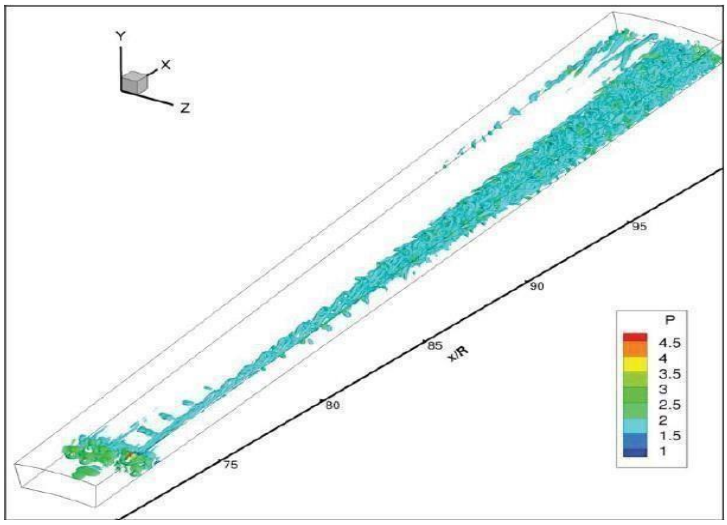

Figure 1.2 Streamwise vortices over roughness distributed at long distances.

Vikram et al. [8] studied the two-dimensional laminar supersonic flow over a flat plate with surface protrusion. They calculated the flow field by calculating the Navier-Stokes equations using the finite difference method. The study suggested that the oblique shock structure and strength are influenced by all the variables [8] to varying extents and having the protrusions as far as possible from the leading edge is recommended as the increasing Reynolds number maximizes the force magnitude [8]. Davide et al. [9] studied supersonic turbulent channel flows over cubic roughness cells using the DNS method. According to this research, the relative drag increase is always greater than the relative heat transfer. However, the increase in Mach number brings the data closer to the Reynolds analogy due to increased aerodynamic heating [9]. Supersonic and hypersonic vehicles use thermal protection systems due to their high thermal environment operations. This layer can be removed due to ablation and when it does, it causes cross-hatching and non-uniform roughness on the surface [9]. Brian et al. [10] investigated the effect of this roughness to characterize quantitatively the aerodynamic effect on the boundary layer. They tested three models one has no roughness, one with uniform diamond roughness, and the other has some random roughness

distribution. PIV and Schlieren were the methods employed for this experiment. They concluded from the experiment that the Reynolds stress is highest in the near wall region for all roughness models [10]. In the study conducted by Guillaume P. et al. [11], wall roughness effects were studied on combustion development in confined supersonic flow. Both reactive and non-reactive RANS simulations of hydrogen injection into a confined transverse supersonic flow were conducted. It was found that the combustion stabilization mechanism changes dramatically regardless of the roughness value [11]. Roughness can be measured with a single scaling parameter and is given by equivalent sand grain roughness height, ks [12]. The empirical correlation calculations were reviewed in the paper by M. Kadivar et al. [12]. The formation of secondary flow is formed due to the roughness, and it is related to the Reynolds stress inhomogeneities that lead to the thickening of boundary layer thickness in the cross-plane of the boundary layer [12].

1.3 Project Objective

The project objective is to evaluate the impact of surface roughness on a thin airfoil on aerodynamic parameters such as lift, drag, and thermal properties and compare the accuracy of results with different software.

1.4 Methodology

This project will be carried out in both theoretical and computational analysis. For the theoretic approach, the fundamental governing equations involving the continuity, momentum, and energy equations shall be used, and then proceed with the non-dimensional analysis. This analytical approach will provide a basic theoretical framework. For the computational analysis part, the airfoil will be designed in SolidWorks with the surface roughness distribution and the analysis will be done using ANSYS and Star CCM+ following which the results from the references will be used for the validation of obtained results. The study is based on real-life situations and thus it utilizes parameters such as viscosity, thermal, etc. This study will be done with different proposed cases which are 1. Top surface roughness, 2. Bottom surface roughness, 3. Leading edge roughness, 4. Trailing edge roughness, 5. Alternative roughness with leading roughness on top and trailing edge roughness on bottom, 6. Alternative roughness with trailing edge roughness on top and leading-edge roughness on bottom. A fine mesh would be used to simulate the flow with unstructured triangular mesh. These triangular elements are chosen for the meshing because of the curved geometry design of the airfoil. The triangular element method provides better results than the structured mesh as the numerical diffusion is greater than other types [13]. For the solvers, the RANS solver will be used to solve the Navier-Stokes equation for the simulation of the flow at near-wall conditions. Since the simulation is in the 2D domain, the z components are eliminated in the momentum, continuity, and energy equations. In the future, this work will be extended to three-dimensional analysis.

2 Geometric Design

For this project, the NACA 64-008 symmetric airfoil is considered for the airfoil design and the shape of this airfoil is very thin and is of diamond wedge shape. This airfoil has a thickness-to-chord ratio of 6% which is very well suitable for supersonic applications. The top layer of the surface is modified by inhibiting the roughness elements.

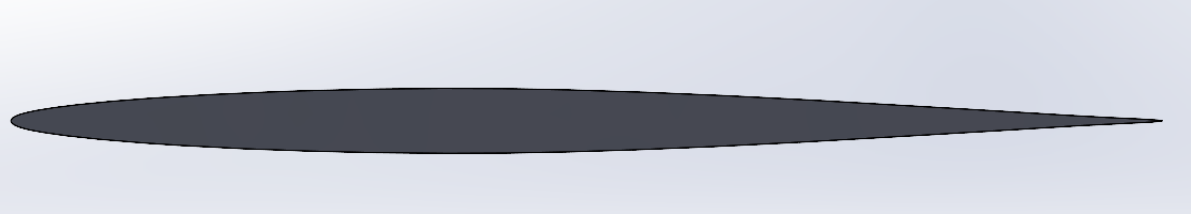

Figure 2.1 NACA 64-008 airfoil

2.1 Roughness elements

The roughness elements on supersonic airfoils have a complex role in impacting aerodynamic performance, stability, and heat transfer. In supersonic flow, delaying the flow separation is very important to optimize the lift and drag generation. So, these roughness elements when placed strategically, can be used to control the transition from laminar to turbulent flow at the desired location on the airfoil. The size and distribution of the roughness elements are crucial in creating impacts. The small-sized elements will only affect the local boundary layer flow whereas the larger elements influence overall airfoil performance.

2.1.1 Surface Topology

The roughness elements are distributed over the surface of the airfoil in different configurations near the leading edge where the boundary layer gets separated at high angles of attack. These elements are designed in different shapes and sizes. The wavelength of the roughness elements is taken as 2.18mm and the height is approximately 0.559mm to 1mm. The shape of these elements was sketched as triangular and rectangular configurations.

Figure 2.2 Roughness elements distribution

The airfoil will be analyzed in the 2D domain under viscous compressible flow. The two cases which are smooth surfaced airfoil and rough surfaced airfoil will be compared with the results for their basic aerodynamic parameters such as lift, drag, pitch moment, etc. The ANSYS Fluent solver will be used to simulate the experiment with the k-Epsilon (2 - equation) realizable model. This model will allow us to capture the flow near the wall boundary where the boundary layer physics occurs.

3 Theoretical Analysis of the Flow Field

The conservation equations of mass, momentum, and energy for the compressible flow of Newtonian fluid are given by
Continuity:

$$\frac{\partial \rho}{\partial t} + \rho\left(\frac{\partial u}{\partial x} + \frac{\partial v}{\partial y}\right) = 0 \tag{3.1}$$

Momentum:
In X-direction:

$$\rho\left(u\frac{\partial u}{\partial x} + v\frac{\partial u}{\partial y}\right) = -\frac{\partial p}{\partial x} + \mu\left(\frac{\partial^2 u}{\partial x^2} + \frac{\partial^2 u}{\partial y^2}\right) \tag{3.2}$$

In Y-direction:

$$\rho\left(u\frac{\partial v}{\partial x} + v\frac{\partial v}{\partial y}\right) = -\frac{\partial p}{\partial y} + \mu\left(\frac{\partial^2 v}{\partial x^2} + \frac{\partial^2 v}{\partial y^2}\right) \tag{3.3}$$

Energy:

$$\rho\left(u\frac{\partial\left(e+\frac{U^2}{2}\right)}{\partial x} + v\frac{\partial\left(e+\frac{U^2}{2}\right)}{\partial y}\right) = -p\left(\frac{\partial u}{\partial x} + \frac{\partial v}{\partial y}\right) + k\left(\frac{\partial^2 T}{\partial x^2} + \frac{\partial^2 T}{\partial y^2}\right) + \frac{\partial}{\partial y}\left(\mu\left(\frac{\partial v}{\partial x} + \frac{\partial u}{\partial y}\right)\right) \tag{3.4}$$

And is reduced by considering the following assumptions:

- The flow is compressible.
- The flow is steady.
- Flow is fully developed in x-direction.
- 2-Dimensional viscous flow

Continuity:
For a fully developed flow in x-direction, there are no changes in flow variables in that direction. Thus, the equation becomes:

$$\rho\frac{\partial v}{\partial y} = 0 \tag{3.5}$$

Momentum in x- direction:

$$\rho\left(u\frac{\partial u}{\partial x} + v\frac{\partial v}{\partial y}\right) = -\frac{\partial p}{\partial x} + \mu\left(\frac{\partial^2 u}{\partial x^2} + \frac{\partial^2 u}{\partial y^2}\right) \tag{3.6}$$

considering the assumptions, the equation reduces to,

$$0 = -\frac{\partial p}{\partial x} + \mu\left(\frac{\partial^2 u}{\partial y^2}\right) \tag{3.7}$$

Since the steady flow cancels out the temporal term and the fully developed flow makes no changes in the flow variables, hence makes the x derivatives zero.

Momentum in y-direction:

Like the x momentum equation, in the y- direction the conservation equation states as

$$\rho\left(u\frac{\partial v}{\partial x} + v\frac{\partial v}{\partial y}\right) = -\frac{\partial p}{\partial y} + \mu\left(\frac{\partial^2 v}{\partial x^2} + \frac{\partial^2 v}{\partial y^2}\right) \tag{3.8}$$

and when applying the above-mentioned assumptions, we get: -

$$\rho\left(v\frac{\partial v}{\partial y}\right) = -\frac{\partial p}{\partial y} + \mu\left(\frac{\partial^2 v}{\partial x^2} + \frac{\partial^2 v}{\partial y^2}\right) \tag{3.9}$$

Energy:

$$\rho\left(u\frac{\partial\left(e+\frac{U_\infty^2}{2}\right)}{\partial x} + v\frac{\partial\left(e+\frac{U_\infty^2}{2}\right)}{\partial y}\right) = -p\left(\frac{\partial u}{\partial x} + \frac{\partial v}{\partial y}\right) + k\left(\frac{\partial^2 T}{\partial x^2} + \frac{\partial^2 T}{\partial y^2}\right) + \frac{\partial}{\partial y}\left(\mu\left(\frac{\partial v}{\partial x} + \frac{\partial u}{\partial y}\right)\right) \tag{3.10}$$

where e is the internal energy and $\frac{U_\infty^2}{2}$ is the kinetic energy. Considering the assumptions, the equation can be reduced as:

$$\rho\left(v\frac{\partial\left(e+\frac{U_\infty^2}{2}\right)}{\partial y}\right) = -p\left(\frac{\partial u}{\partial x} + \frac{\partial v}{\partial y}\right) + \frac{\partial}{\partial y}\left(k\frac{\partial T}{\partial y}\right) + \frac{\partial}{\partial y}\left(\mu\frac{\partial u}{\partial y}\right) \tag{3.11}$$

3.1 Non-Dimensional Analysis

Non-dimensioning the governing equations will generate an easy approach to identifying the dimensionless parameters that govern the flow behavior. The non-dimensional velocities, spatial coordinates, and pressure are introduced as:

$$\bar{u} = \frac{\bar{\bar{u}}}{U_\infty}$$
$$\bar{v} = \frac{v}{U_\infty}$$
$$\bar{x} = \frac{x}{L}$$
$$\bar{y} = \frac{y - \delta}{\delta}$$
$$\bar{p} = \frac{p - p_\infty}{p_o - p_\infty}$$
$$\bar{T} = \frac{T - T_\infty}{T_o - T_\infty}$$
$$\bar{e} = \frac{e}{C_v T_\infty}$$
$$\overline{U_\infty^2} = \frac{U^2}{U_\infty^2} = \frac{u^2 + v^2}{U_\infty^2}$$

Continuity:

$$\frac{\rho U_\infty}{L}\frac{\partial \bar{v}}{\partial \bar{y}} = 0 \tag{3.12}$$

Momentum in x-direction:

$$\frac{\rho U_\infty^2 \bar{v}}{L}\left(\frac{\partial \bar{u}}{\partial \bar{y}}\right) = -\frac{1}{L}(p_\infty + (p_0 - p_\infty)\bar{p})\frac{\partial \bar{p}}{\partial \bar{x}} + \mu\left(\frac{U_\infty}{L^2}\frac{\partial^2 \bar{u}}{\partial \bar{y}^2}\right) \tag{3.13}$$
$$\bar{v}\left(\frac{\partial \bar{u}}{\partial \bar{y}}\right) = -\frac{1}{\rho U_\infty^2}(p_\infty + (p_0 - p_\infty)\bar{p})\frac{\partial \bar{p}}{\partial \bar{x}} + \frac{\mu}{\rho U_\infty L}\left(\frac{\partial^2 \bar{u}}{\partial \bar{y}^2}\right) \tag{3.14}$$

here, $\frac{P_\infty}{\rho U_\infty^2} = \frac{a^2}{\gamma U_\infty^2} = \frac{1}{\gamma M_\infty^2}$, $\frac{\mu}{\rho U_{\infty L}} = \frac{1}{Re}$ and, $v = 0$

$$0 = -\left(\frac{1}{\gamma M_\infty^2} + \frac{(p_0 - p_\infty)\bar{p}}{\rho U_\infty^2}\right)\frac{\partial \bar{p}}{\partial \bar{x}} + \frac{1}{Re}\left(\frac{\partial^2 \bar{u}}{\partial \bar{y}^2}\right) \tag{3.15}$$

Momentum in y-direction:

$$\frac{\rho U_\infty^2 \bar{v}}{L}\left(\frac{\partial \bar{v}}{\partial \bar{y}}\right) = -\frac{1}{L}(p_\infty + (p_0 - p_\infty)\bar{p})\frac{\partial \bar{p}}{\partial \bar{x}} + \mu\left(\frac{U_\infty}{L^2}\frac{\partial^2 \bar{v}}{\partial \bar{y}^2}\right) \tag{3.16}$$
$$\bar{v}\left(\frac{\partial \bar{v}}{\partial \bar{y}}\right) = -\frac{1}{\rho U_\infty^2}(p_\infty + (p_o - p_\infty)\bar{p})\frac{\partial \bar{p}}{\partial \bar{x}} + \frac{\mu}{\rho U_\infty L}\left(\frac{\partial^2 \bar{v}}{\partial \bar{y}^2}\right) \tag{3.17}$$

here, $\frac{P_\infty}{\rho U_\infty^2} = \frac{a^2}{\gamma U_\infty^2} = \frac{1}{\gamma M_\infty^2}$, $\frac{\mu}{\rho U_{\infty L}} = \frac{1}{Re}$ and $v = 0$

$$0 = -\left(\frac{1}{\gamma M_\infty^2} + \frac{(p_0 - p_\infty)\bar{p}}{\rho U_\infty^2}\right)\frac{\partial \bar{p}}{\partial x} + \frac{1}{Re}\left(\frac{\partial^2 \bar{u}}{\partial y^2}\right) \tag{3.18}$$

Energy:

$$\begin{aligned} &\frac{T_\infty \rho_\infty \bar{\rho} C_v U_\infty \bar{v}}{L}\frac{\partial \bar{e}}{\partial \bar{y}} + \frac{\rho_\infty U_\infty^3}{2L}\bar{\rho}\bar{v}\frac{\partial(\bar{u}^2 + \bar{v}^2)}{\partial \bar{y}} = -(p_\infty + (p_o - p_\infty)\bar{p})\frac{U_\infty}{L}\left(\frac{\partial \bar{u}}{\partial \bar{x}} + \frac{\partial \bar{v}}{\partial \bar{y}}\right) \\ &\bar{\rho}\bar{v}\frac{\partial \bar{e}}{\partial \bar{y}} = -\frac{U_\infty^2}{2T_\infty C_v}\bar{\rho}\bar{v}\frac{\partial(\bar{u}^2 + \bar{v}^2)}{\partial \bar{y}} - \frac{(p_\infty + (p_o - p_\infty)\bar{p})}{T_\infty C_v \rho_\infty}\left(\frac{\partial \bar{v}}{\partial \bar{y}}\right) + \frac{k_\infty}{L U_\infty C_v \rho_\infty}\frac{\partial}{\partial \bar{y}}\left(\bar{k}\frac{\partial \bar{T}}{\partial \bar{y}}\right) \end{aligned} \tag{3.19}$$

Coefficients of each term on the RHS can be rewritten in terms of Mach number, Reynold's number and Prandtl number as:

$$\frac{U_\infty^2}{2T_\infty C_v} = \frac{(\gamma - 1)U_\infty^2}{RT_\infty} = \frac{\gamma(\gamma - 1)U_\infty^2}{\gamma R T_\infty} = \frac{\gamma(\gamma - 1)U_\infty^2}{a_\infty^2} = \gamma(\gamma - 1)M_\infty^2 \tag{3.20}$$

where $C_p = C_v + R$ and $\gamma = \frac{C_p}{C_v}$ which gives, $C_v = \frac{R}{(\gamma - 1)}$;

$$\begin{aligned} &\frac{T_\infty \rho_\infty \bar{\rho} C_v U_\infty \bar{v}}{L}\frac{\partial \bar{e}}{\partial \bar{y}} + \frac{\rho_\infty U_\infty^3}{2L}\bar{\rho}\bar{v}\frac{\partial(\bar{u}^2 + \bar{v}^2)}{\partial \bar{y}} = -(p_\infty + (p_o - p_\infty)\bar{p})\frac{U_\infty}{L}\left(\frac{\partial \bar{u}}{\partial \bar{x}} + \frac{\partial \bar{v}}{\partial \bar{y}}\right) \\ &\bar{\rho}\bar{v}\frac{\partial \bar{e}}{\partial \bar{y}} = -\frac{U_\infty^2}{2T_\infty C_v}\bar{\rho}\bar{v}\frac{\partial(\bar{u}^2 + \bar{v}^2)}{\partial \bar{y}} - \frac{(p_\infty + (p_o - p_\infty)\bar{p})}{T_\infty C_v \rho_\infty}\left(\frac{\partial \bar{v}}{\partial \bar{y}}\right) + \frac{k_\infty}{L U_\infty C_v \rho_\infty}\frac{\partial}{\partial \bar{y}}\left(\bar{k}\frac{\partial \bar{T}}{\partial \bar{y}}\right) \end{aligned} \tag{3.21}$$

Coefficients of each term on the RHS can be rewritten in terms of Mach number, Reynold's number and Prandtl number as:

$$\frac{U_\infty^2}{2T_\infty C_v} = \frac{(\gamma - 1)U_\infty^2}{RT_\infty} = \frac{\gamma(\gamma - 1)U_\infty^2}{\gamma R T_\infty} = \frac{\gamma(\gamma - 1)U_\infty^2}{a_\infty^2} = \gamma(\gamma - 1)M_\infty^2 \tag{3.22}$$

where $C_p = C_v + R$ and $\gamma = \frac{C_p}{C_v}$ which gives, $C_v = \frac{R}{(\gamma - 1)}$;

The energy equation can be written in terms of Mach number, Reynold's Number, and Prandtl Number as:

$$\begin{aligned} \bar{\rho}\bar{v}\frac{\partial \bar{e}}{\partial \bar{y}} = -\gamma(\gamma - 1)M_\infty^2 \bar{\rho}\bar{v}\frac{\partial(\bar{u}^2 + \bar{v}^2)}{\partial \bar{y}} - (\gamma - 1)\left(\frac{(p_o - p_\infty)\bar{p}}{P_\infty} + 1\right)\left(\frac{\partial v}{\partial y}\right) + \frac{k\gamma}{Pr_\infty Re_\infty}\frac{\partial^2 \bar{T}}{\partial \bar{y}^2} \\ + \frac{\gamma(\gamma - 1)M_\infty^2}{Re_\infty^2}\frac{\partial^2 \bar{u}}{\partial \bar{y}^2} \end{aligned} \tag{3.23}$$

dividing the entire equation by $(\gamma - 1)$, we get

$$\bar{\rho}\bar{v}\frac{\partial \bar{e}}{\partial \bar{y}} = -\gamma M_{\infty}^{2}\bar{\rho}\bar{v}\frac{\partial(\bar{u}^{2}+\bar{v}^{2})}{\partial \bar{y}} - \left(\frac{(p_o - p_{\infty})\bar{p}}{P_{\infty}} + 1\right)\left(\frac{\partial \bar{v}}{\partial \bar{y}}\right) + \frac{k\gamma}{Pr_{\infty}Re_{\infty}}\frac{1}{(\gamma-1)}\frac{\partial^{2}\bar{T}}{\partial \bar{y}^{2}} \quad (3.24)$$

These non-dimensional equations highlight the Mach number, Reynolds number, Prandtl number, the specific heat ratio on the flow, and the heat transfer behavior around the airfoil. These equations shall be used by the solver to simulate the model under certain boundary conditions.

4 Grid generation and Boundary Conditions

The domain for the grid generation is of C-type and unstructured triangular mesh has been used for better accuracy of results for this roughness geometry. The domain is split into 6 faces to refine the mesh elements at the required positions. Using the sizing control the refinement is adjusted as per the requirement. Inflation is used around the airfoil to obtain the maximum data possible. The total number of elements of the final mesh is 302700. To validate the mesh quality, a mesh independence study is done with three versions of the same mesh: Coarse, medium, and fine. By a factor of 1.414, the number of elements is altered according to the refinement.

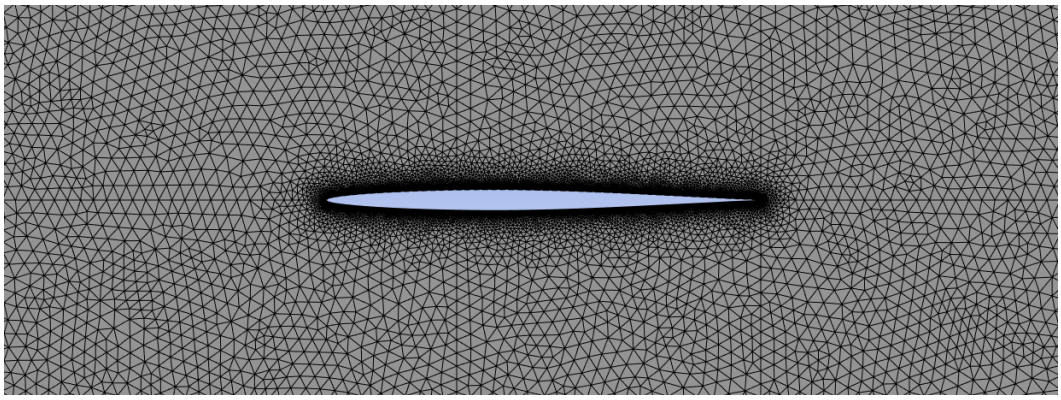

Figure 4.1 Unstructured triangular mesh

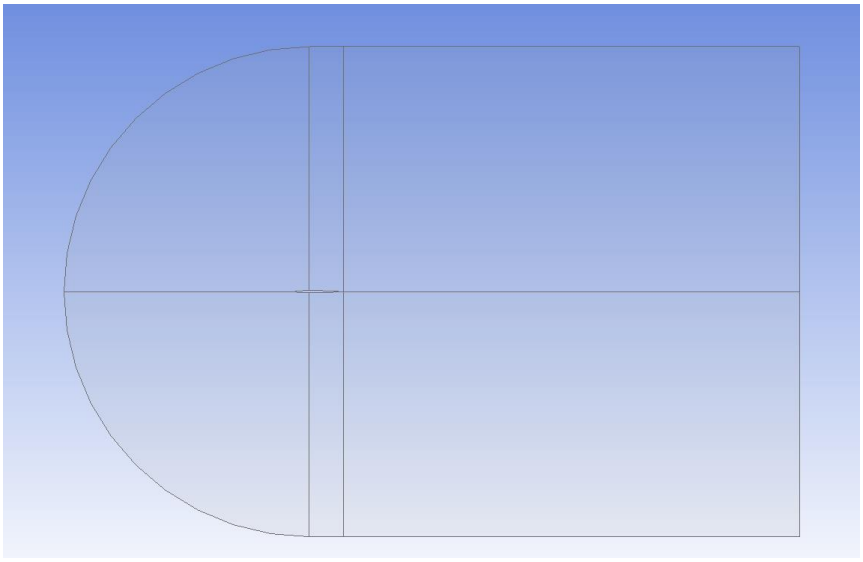

Figure 4.2 C-type domain

4.1 Boundary Conditions

The simulation is in a supersonic regime and hence the solver type used is density-based. The model used for this near-wall condition geometry is K-epsilon (2-eqn). The properties of the flow field are defined below.

Table 4.1 Boundary conditions

Inlet - Pressure far field	Density - Ideal Gas
	Viscosity – Sutherland Three coefficient method
	Mach Number – 2.0
Outlet – Pressure Outlet	Guage pressure – 0
Airfoil- Wall	No-slip

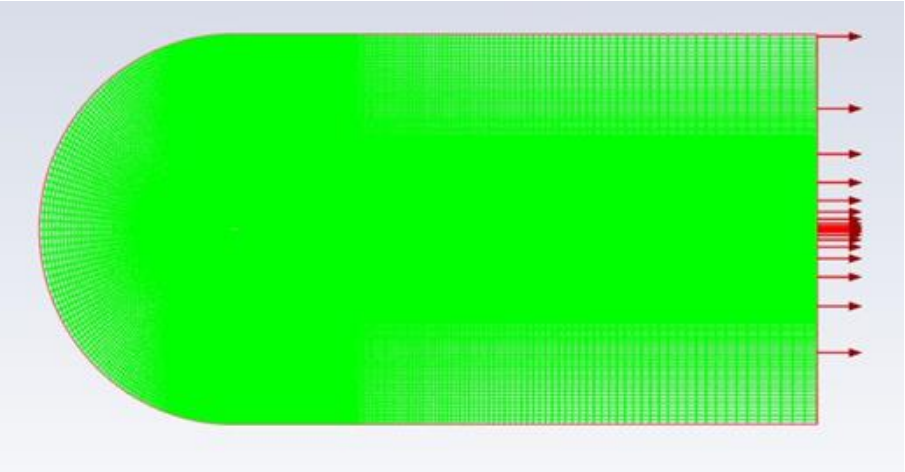

Figure 4.3 Domain setup

With the following boundary conditions, the mesh independence study was done, and the results were compared with the work of Madhanraj et al. 2023. The results obtained from the three types are similar to the reference values and hence the mesh is of good quality and independent of the mesh refinement.

Table 4.2 Mesh Independence Study

AOA = 5 deg	**Coarse Mesh**	**Medium Mesh**	**Fine Mesh**	**Reference Data**
C_L	0.207	0.202	0.198	0.29
C_D	0.03	0.028	0.03	0.03

The simulation was computed from the inlet with a velocity of 638 m/s and was run for 4000 iterations at which the solution was converged.

5 Results and Discussion

The results were obtained from the simulations for all six designs and were compared with the baseline smooth airfoil design. The parameters used for comparison are the coefficient of lift, the coefficient of drag, and the angle of attack. These are the nondimensional numbers independent of the free stream velocity and were evaluated with the 1000 mm chord length of the airfoil. Table 5.1 lists the value obtained for the zero angle of attack. The comparison and analysis are discussed below.

Table 5.1 Data analysis of aerodynamic parameter for 0^o angle of attack.

Design	Lift (N)	Drag (N)	C_L	C_D	C_L/C_D
Smooth surface	1.5069301	3223.7798	7.81E-06	0.016698045	4.67E-04
Top Layer Roughness	-0.00722	17603.32	-0.00722	0.036937	-0.19538
Bottom Layer Roughness	2971.723	14146.04	0.006236	0.029683	0.210075
Leading Edge Roughness	-408.999	6498.179	-0.00212	0.033658	-0.06294
Trailing Edge Roughness	-218.175	5741.268	-0.00113	0.029738	-0.038
Leading Edge Top roughness, Trailing Edge Bottom Roughness	-125.246	8439.757	-0.00026	0.017709	-0.01484
Leading Edge Bottom roughness, Trailing Edge Top Roughness	279.4467	8103.965	0.001447	0.041976	0.034483

From the table above, it can be observed that the lift generated by the baseline design is 1.509 N whereas the bottom roughness design produces 2972 N of lift which is the highest among all designs. The drag produced by the top surface is about 17603 N which is the highest among the designs. On calculating the CL and CD, the bottom surface generates the highest CL/CD ratio which is 0.21. The pressure and Mach number contours are displayed below.

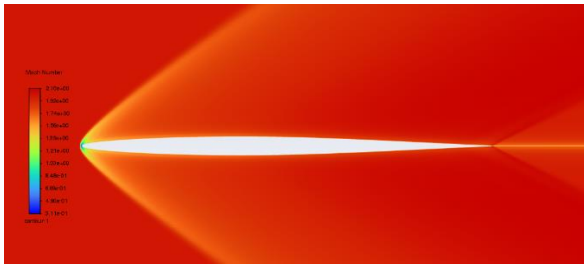

Figure 5.1 Smooth surface Mach contour

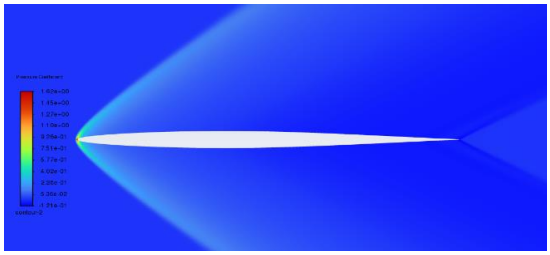

Figure 5.2 Smooth surface pressure contour

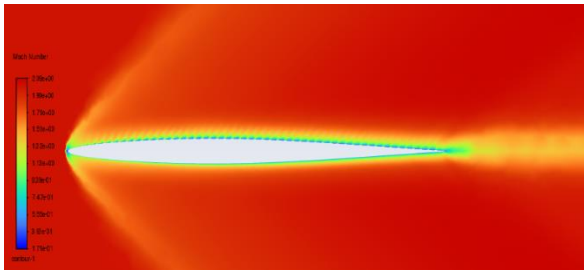

Figure 5.3 Top roughness Mach contour

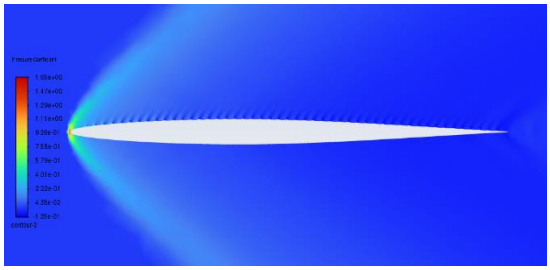

Figure 5.4 Top roughness pressure contour

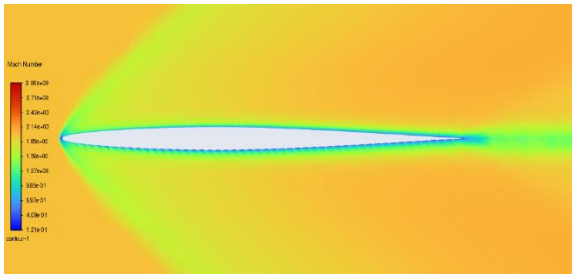

Figure 5.5 Bottom roughness Mach contour

Figure 5.6 Bottom roughness pressure contour

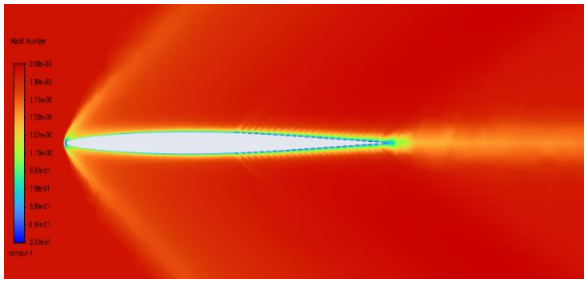

Figure 5.7 Trailing edge roughness Mach contour

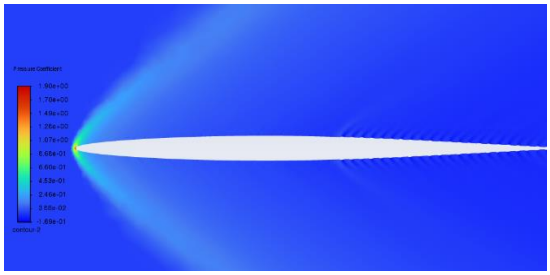

Figure 5.8 Trailing edge roughness pressure contour

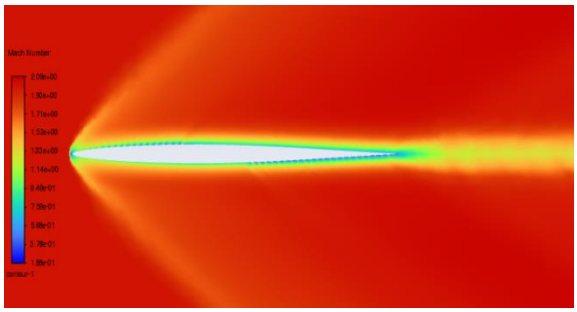

Figure 5.9 LE_top roughness Mach contour

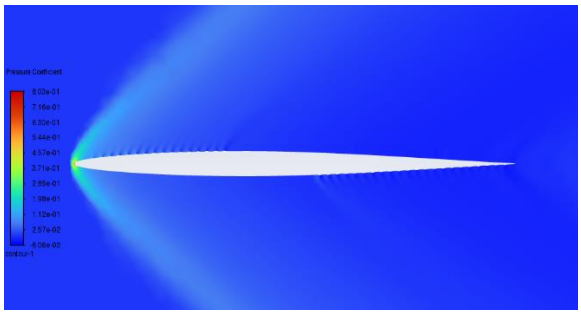

Figure 5.10 LE_top roughness pressure contour

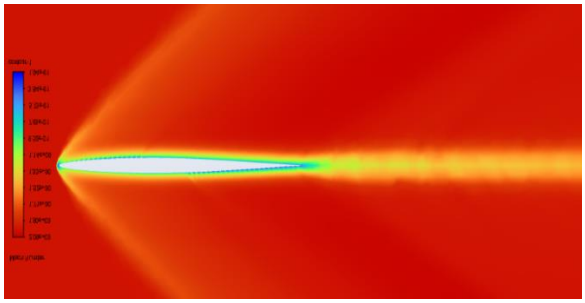

Figure 5.11 TE_top roughness Mach contour

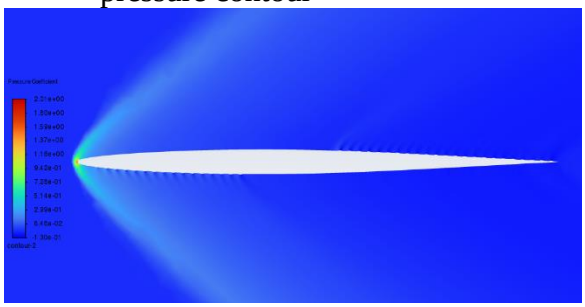

Figure 5.12 TE_top roughness pressure contour

Table 5.2 discusses the aerodynamic data for the angle of attack of 3^{o} and the results are compared and analyzed below.

Table 5.2 Data analysis of aerodynamic parameters for 3^{o} angle of attack.

Design	Lift (N)	Drag (N)	C_L	C_D	C_L/C_D
Smooth surface	23297.08	3199.291	0.120671	0.016571	7.281951
Top Layer Roughness	53825.26	17382.96	0.112942	0.036475	3.096439
Bottom Layer Roughness	59380.08	14079.16	0.124598	0.029543	4.217588

Table 5.2 Data analysis of aerodynamic parameters for 3° angle of attack. (contd.)

Leading Edge Roughness	22928.43	6441.47	0.118761	0.033365	3.559502
Trailing-Edge Roughness	23288.09	5687.385	0.120624	0.029459	4.094692
Leading Edge Top roughness, Trailing Edge Bottom Roughness	23684.55	8406.139	0.049698	0.017639	2.81753
Leading Edge Bottom roughness, Trailing Edge Top Roughness	23731.84	8038.008	0.122923	0.041634	2.952453

Here the top and bottom surfaces produce high lift force but due to their high density produced because of the strong shocks and high-pressure difference, the CL and CD are lower comparatively. Therefore, the smooth design produces the highest CL/CD ratio. The contours of pressure and Mach number are displayed below.

Figure 5.13 Smooth surface Mach contour

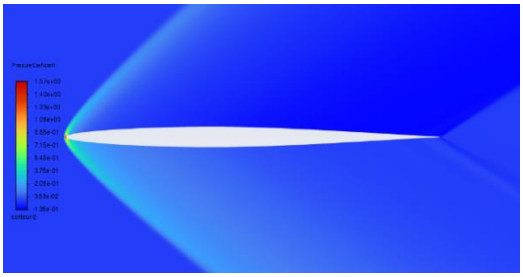

Figure 5.14 Smooth surface pressure contour

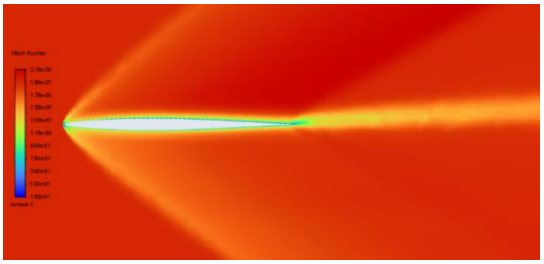

Figure 5.15 Top roughness Mach contour

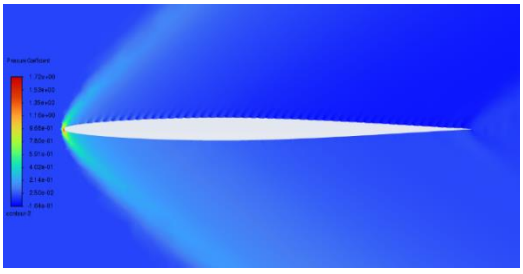

Figure 5.16 Top roughness pressure contour

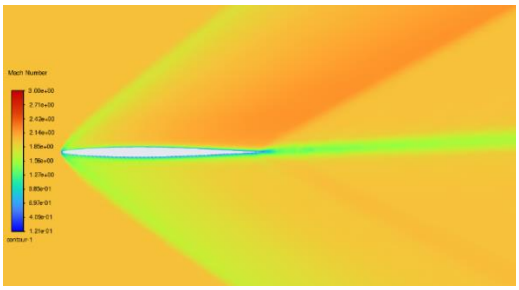

Figure 5.17 Bottom roughness Mach contour

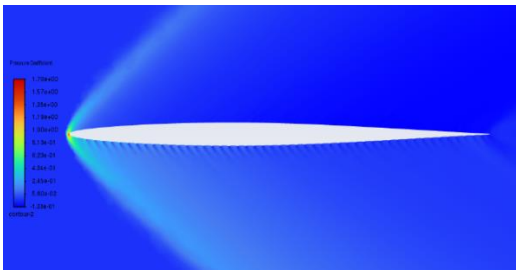

Figure 5.18 Bottom roughness pressure contour

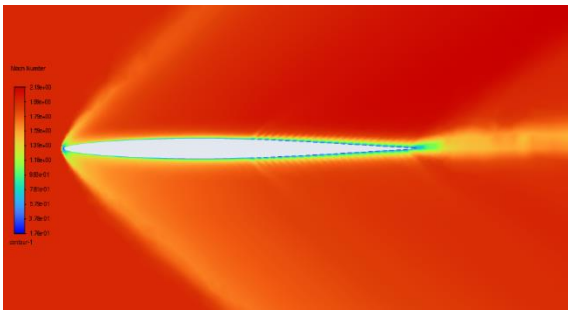

Figure 5.19 Trailing edge roughness Mach contour

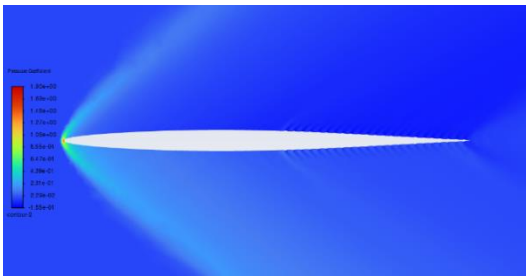

Figure 5.20 Trailing edge roughness pressure contour

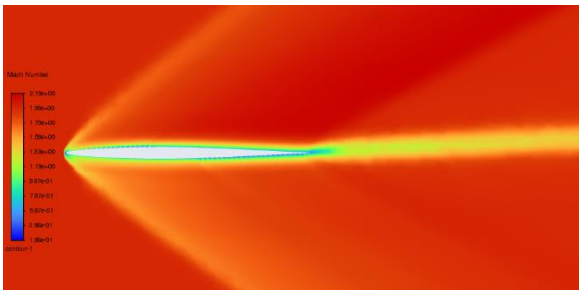

Figure 5.21 LE_top roughness Mach contour

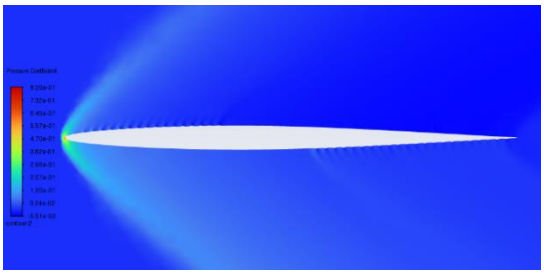

Figure 5.22 LE_top roughness pressure contour

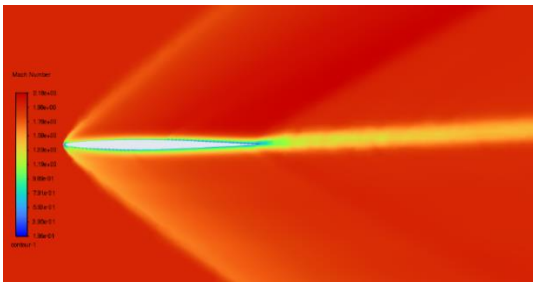

Figure 5.23 TE_top roughness Mach contour

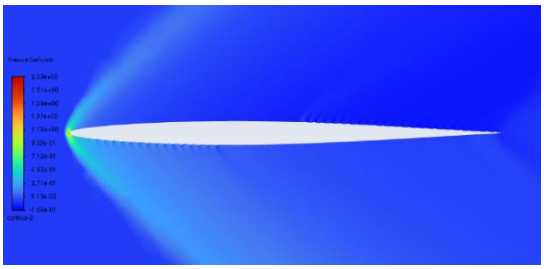

Figure 5.24 TE_top roughness pressure contour

Table 5.3 discusses the aerodynamic parameters of all the design points for a 6^o angle of attack.

Table 5.3 Data analysis of aerodynamic parameters for 6^o angle of attack.

Design	Lift (N)	Drag (N)	C_L	C_D	C_L/C_D
Smooth surface	46994.93	3168.788	0.243417	0.016413	14.83057
Top Layer Roughness	114534.6	16630.66	0.24033	0.034896	6.886957
Bottom Layer Roughness	116664	13794.93	0.244798	0.028946	8.457023
Leading Edge Roughness	47128.93	6261.56	0.244111	0.032433	7.526706
Trailing Edge Roughness	47287.5	5826.324	0.244933	0.030178	8.116181
Leading Edge Top roughness, Trailing Edge Bottom Roughness	47716.13	8333.513	0.100124	0.017486	5.725813
Leading Edge Bottom roughness, Trailing Edge Top Roughness	47551.09	7908.413	0.246298	0.040963	6.012722

Here the highest lift is produced by the top and bottom layer roughness designs and again the density is higher than the smooth surface hence the coefficient of lift is lesser than the smooth surface. The drag force produced by the top and the bottom layer roughness is relatively smaller than the drag produced by smooth when compared with the lift generation. Therefore, the resulting CL/CD ratio is highest for the smooth-surfaced airfoil. The Mach number and pressure contours are displayed below.

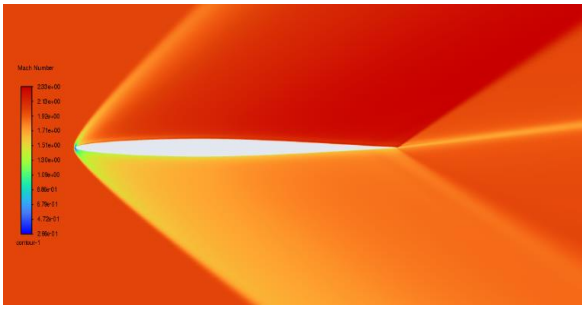

Figure 5.25 Smooth surface Mach contour

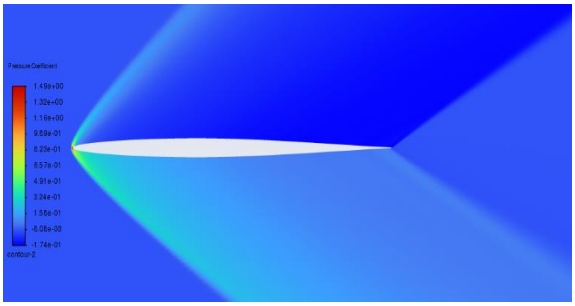

Figure 5.26 Smooth surface pressure contour

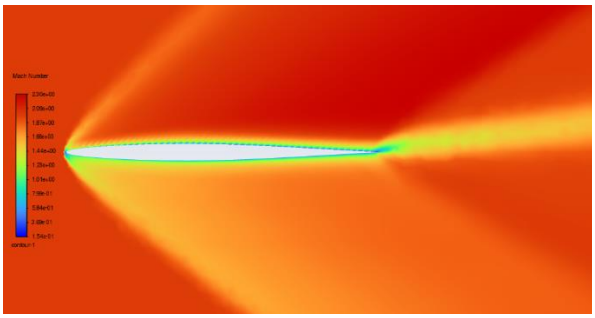

Figure 5.27 Top roughness Mach contour

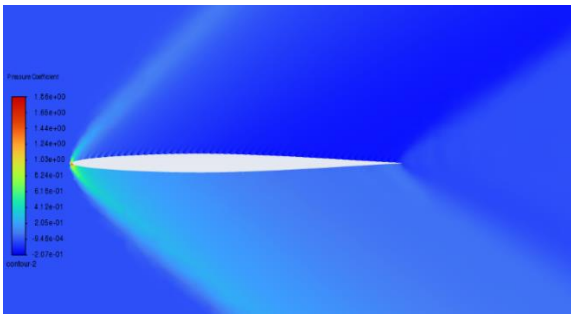

Figure 5.28 Top roughness pressure contour

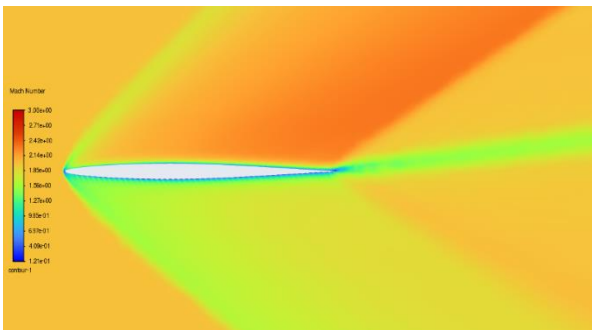

Figure 5.29 Bottom roughness Mach contour

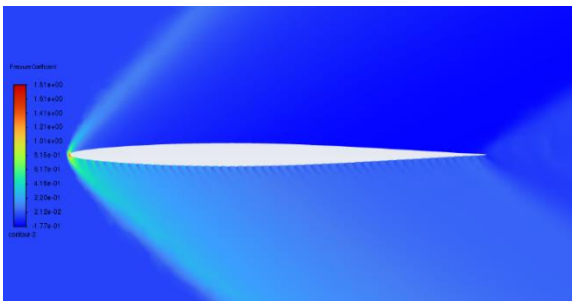

Figure 5.30 Bottom roughness pressure contour

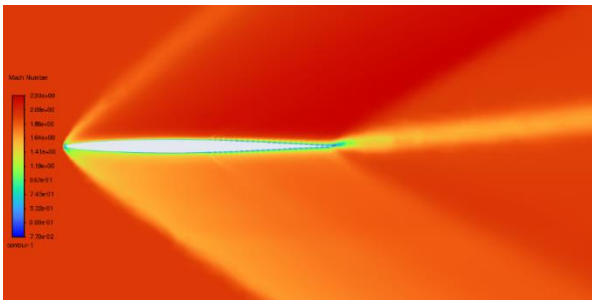

Figure 5.31 Trailing edge roughness Mach contour

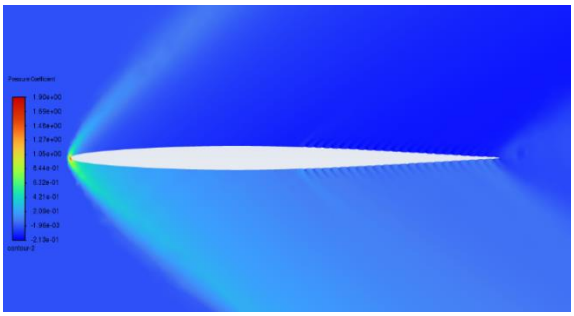

Figure 5.32 Trailing edge roughness pressure contour

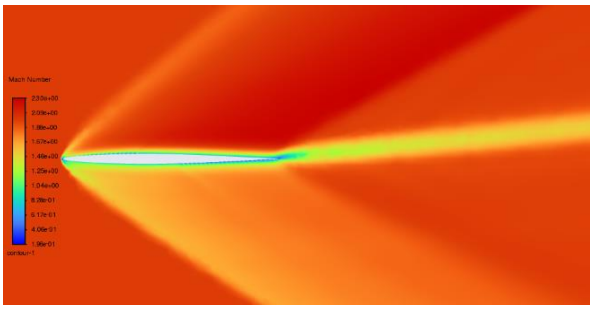

Figure 5.33 LE_top roughness Mach contour

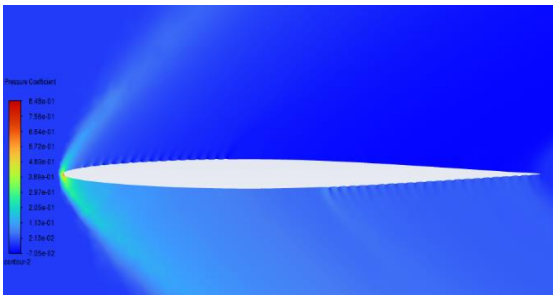

Figure 5.34 LE_top roughness pressure contour

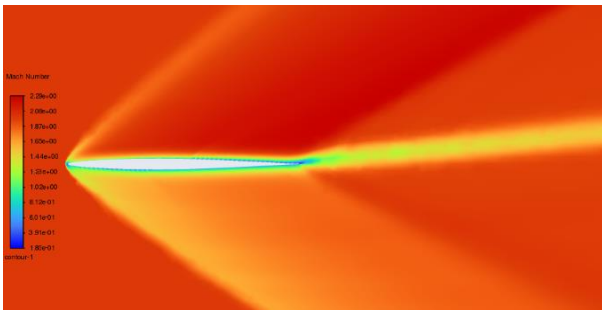

Figure 5.35 TE_top roughness Mach contour

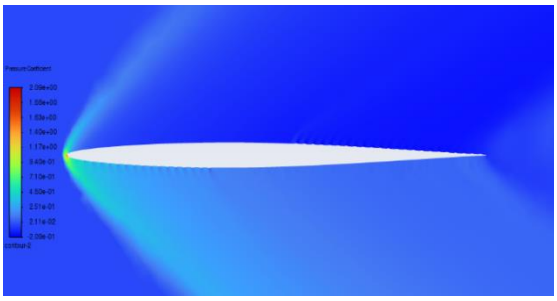

Figure 5.36 TE_top roughness pressure contour

The following table displays the data collected for the aerodynamic parameters for the 9^{o} angle of attack and the comparison and analysis are discussed.

Table 5.4 Data analysis of aerodynamic parameter for 9^{o} angle of attack.

Design	Lift (N)	Drag (N)	CL	CD	CL/CD
Smooth surface	71382.41	3164.298	0.369736	0.01639	22.55869
Top Layer Roughness	175411.6	17130.2	0.368069	0.035945	10.2399
Bottom Layer Roughness	179746	15348.3	0.37002	0.033921	10.9082

Table 5.4 Data analysis of aerodynamic parameter for 9^{o} angle of attack. (contd)

Leading Edge Roughness	72116.42	6612.513	0.373538	0.03425	10.90605
Trailing Edge Roughness	72233.27	6146.592	0.374143	0.031837	11.75176
Leading Edge Top roughness, Trailing Edge Bottom Roughness	72545.97	7975.22	0.152224	0.016735	9.096422
Leading Edge Bottom roughness, Trailing Edge Top Roughness	72973.62	8276.663	0.377978	0.04287	8.816792

The last four designs produce similar lift force, but the drag is higher in the last design. This makes the leading-edge roughness design have the highest CL/CD ratio among the four. The smooth airfoil has a similar lift force, but the drag is less than half of what is produced by the four designs. The top and bottom roughness designs have the highest lift generated and due to its increased density because of the compressibility of air, the coefficients were compromised resulting in a lower CL/CD ratio. The contours of the Mach number and pressure are produced below for comparison.

Figure 5.37 Smooth surface Mach Contour

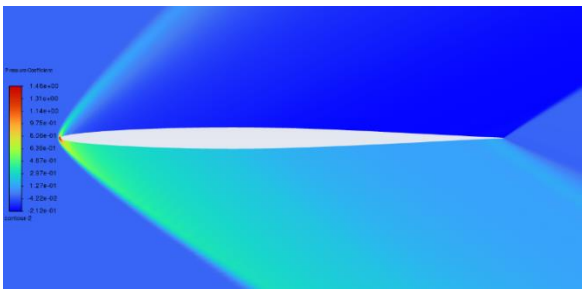

Figure 5.38 Smooth surface pressure contour

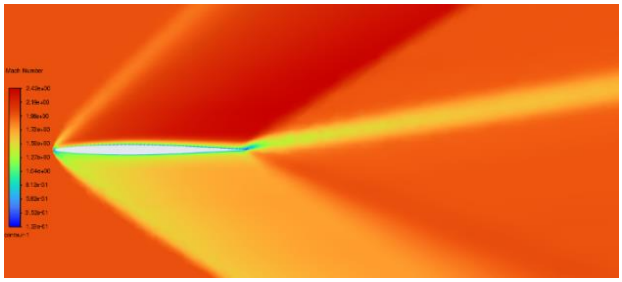

Figure 5.39 Top roughness Mach contour

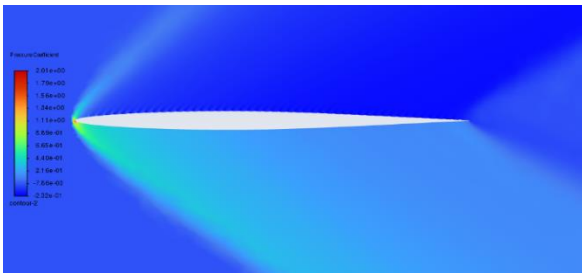

Figure 5.40 Top roughness pressure contour

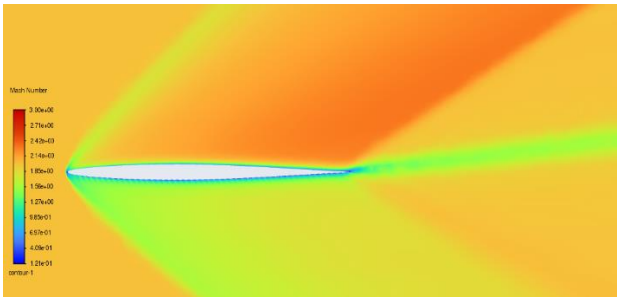

Figure 5.41 Bottom roughness Mach contour

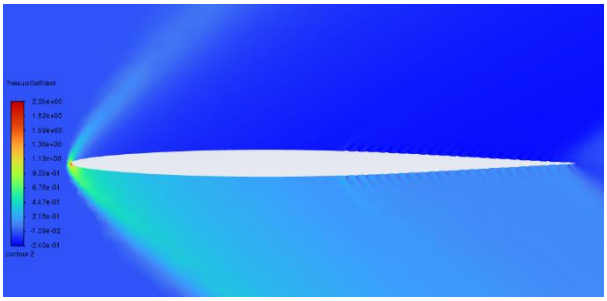

Figure 5.42 Bottom roughness pressure contour

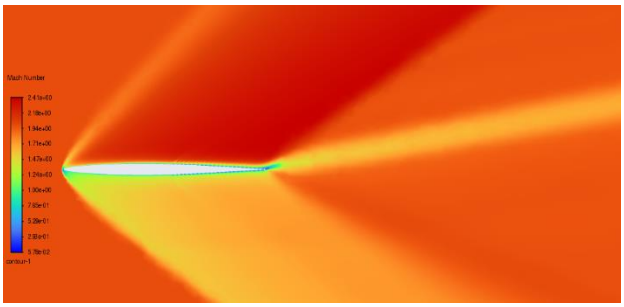

Figure 5.43 Trailing edge roughness Mach contour

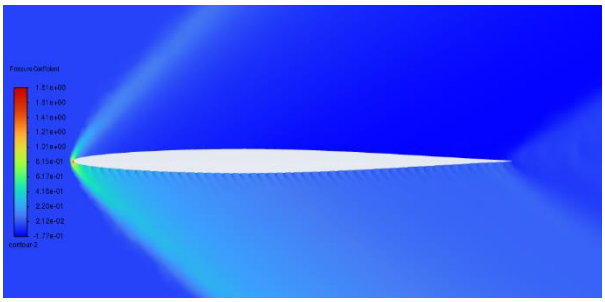

Figure 5.44 Trailing edge roughness pressure contour

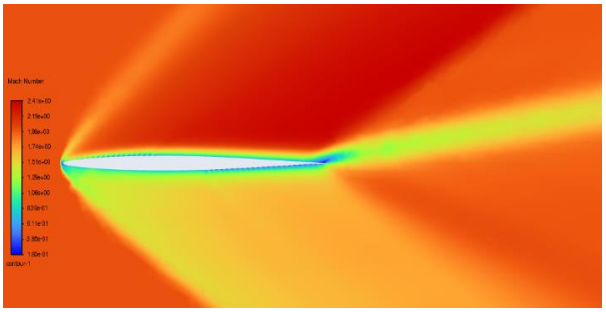

Figure 5.45 LE_top roughness Mach contour

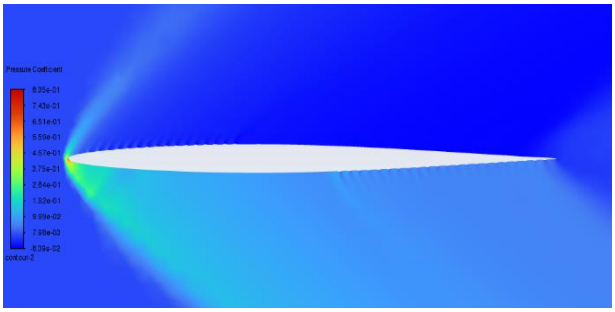

Figure 5.46 LE_top roughness pressure contour

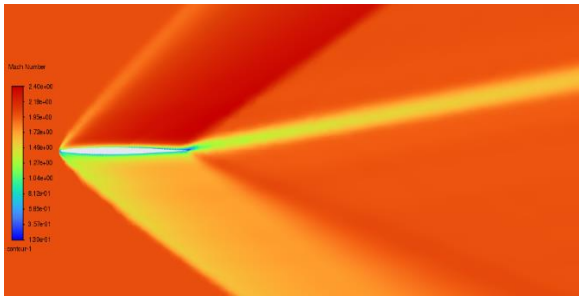

Figure 5.47 TE_top roughness
Mach contour

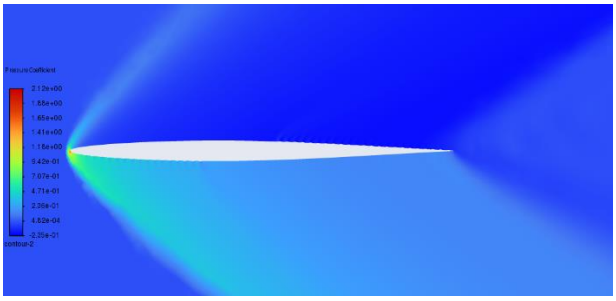

Figure 5.48 TE_top roughness
pressure contour

6 Conclusion

Numerical investigations are carried out to evaluate the lift force, drag force, coefficient of lift, and coefficient of drag for the NACA 64-008 airfoil with roughness placed in six different positions. The experiment was done for α 0^o, 3^o, 6^o, and 9^o and the results were obtained using ANSYS FLUENT. It was observed that the roughness on the surface plays a role in increasing the strength of the shock waves and the pressure coefficient. The roughness on the whole top surface and whole bottom surface makes the airfoil produce more lift force compared to the baseline smooth surface airfoil and when the α is increased, the roughness starts to produce more drag. Therefore, it can be concluded that the influence of roughness on the top and bottom surface of the airfoil produces more lift. The rest of the design produces good lift but also generates more drag making the lift-to-drag ratio drop.

Due to the extensive computational time required for simulations and the restricted time available for this project, the simulations in StarCCM+ were postponed to future studies. To allocate adequate time for thorough investigation and optimization from the ANSYS, this decision was made.

The results of this research offer a critical understanding of how airfoil performance can be optimized by varying surface roughness, especially in instances where more lift is desired. To successfully balance these conflicting aerodynamic forces, however, requires considerable consideration throughout the design phase due to the accompanying rise in drag.

References

[1] Jouybari, M. A., Yuan, J., Li, Z., Brereton, G. J., & Jaberi, F. “Supersonic turbulent flows over sinusoidal rough walls”, *Journal of Fluid Mechanics*, Vol. 956, 2023, pp. A3-1-A3-27. doi:10.1017/jfm.2022.1049.

[2] Latin, R.M., "The Influence of Surface Roughness on Supersonic High Reynolds Number Turbulent Boundary Layer Flow", 1998. Theses and Dissertations. 5509. https://scholar.afit.edu/etd/5509

[3] Van Driest, E. R. “Turbulent boundary layer in compressible fluids.” *Journal of the Aeronautical Sciences (Institute of the Aeronautical Sciences)*, Vol. 19, No. 1, 1952, pp. 55–57.
https://doi.org/10.2514/8.2149.

[4] Fan, H., and Bowersox, R. “Numerical Analysis of high-speed flow over rough surfaces”, 35th Joint Propulsion Conference and Exhibit, Vol. 99, 1999, pp. 2381.

[5] Sharif, M. A. R., and Guo, G. “Computational Analysis of Supersonic Turbulent Boundary Layers over Rough Surfaces Using the k–ω and the Stress–ω Models.” Applied Mathematical Modelling, Vol. 31, No. 12, 2007, pp. 2655–2667.
https://doi.org/10.1016/j.apm.2006.10.007.

[6] Khotyanovsky, D. V., and Kudryavtsev, A. N. “DNS of Surface Roughness Effects on Laminar–Turbulent Transition in a Supersonic Boundary Layer.” Nucleation and Atmospheric Aerosols, Vol.1770, No.1, 2016, pp. 030058.
https://doi.org/10.1063/1.4964000.

[7] Khotyanovsky, D. V., and Kudryavtsev, A. N. “Numerical Study of Surface Roughness Effects in the Boundary Layer of a Blunted Cone in a Supersonic Flow.” Nucleation and Atmospheric Aerosols, Vol.2027, No.1, 2018, pp. 030116.
https://doi.org/10.1063/1.5065210.

[8] Deshpande, V. S., Sanghi, S., and Eshpuniyani, B. “Computational Study of Supersonic Flow Over a Flat Plate with Protrusion.” *Journal Of Aerospace Sciences & Technologies*, Vol.63, No.4,2011,pp.266-276
https://www.researchgate.net/publication/236110524_Computational_Study_of_Supersonic_Flo w_Over_a_Flat_Plate_with_Protrusion

[9] Modesti, D., Sathyanarayana, S., Salvadore, F., and Bernardini, M. “Direct Numerical Simulation of Supersonic Turbulent Flows Over Rough Surfaces.” *Journal of Fluid Mechanics*, Vol. 942, 2022, pp. A44
https://doi.org/10.1017/jfm.2022.393.

[10] Kocher, B. D., Combs, C. S., Kreth, P. A., Schmisseur, J. D., and Peltier, S. “Investigation of the Effects of Distributed Surface Roughness on Supersonic Flows.” 47th AIAA Fluid Dynamics Conference, published online 2 Jun. 2017.
https://doi.org/10.2514/6.2017-4313.

[11] Pelletier, G., Ferrier, M., Vincent-Randonnier, A., Sabelnikov, V., and Mura, A. “Wall Roughness Effects on Combustion Development in Confined Supersonic Flow.” *Journal of Propulsion and Power*, Vol. 37, No. 1, 2021, pp. 151–166. https://doi.org/10.2514/1.b37842.

[12]Kadivar, M., Tormey, D., and McGranaghan, G. “A Review on Turbulent Flow over Rough Surfaces: Fundamentals and Theories.” *International Journal of Thermofluids*, Vol. 10, 2021, p. 100077.
https://doi.org/10.1016/j.ijft.2021.100077.

[13]Madhanraj, V., Saravanan, P., Shankaralingam, L., Balaji, G., SaiBabu, A., Sateesh, R., & Seralathan, S., "Study on aerodynamics characteristics of the effect of leading-edge radius of FDM printed (ABSi material) supersonic aerofoil," Materials Today: Proceedings, published online 25 April 2023.
https://doi.org/10.1016/j.matpr.2023.04.251

Appendix A: Solver Settings

The solver settings used for the simulation are discussed below. For this experiment, the solver is chosen as density-based as the flow is compressible and in a supersonic regime.

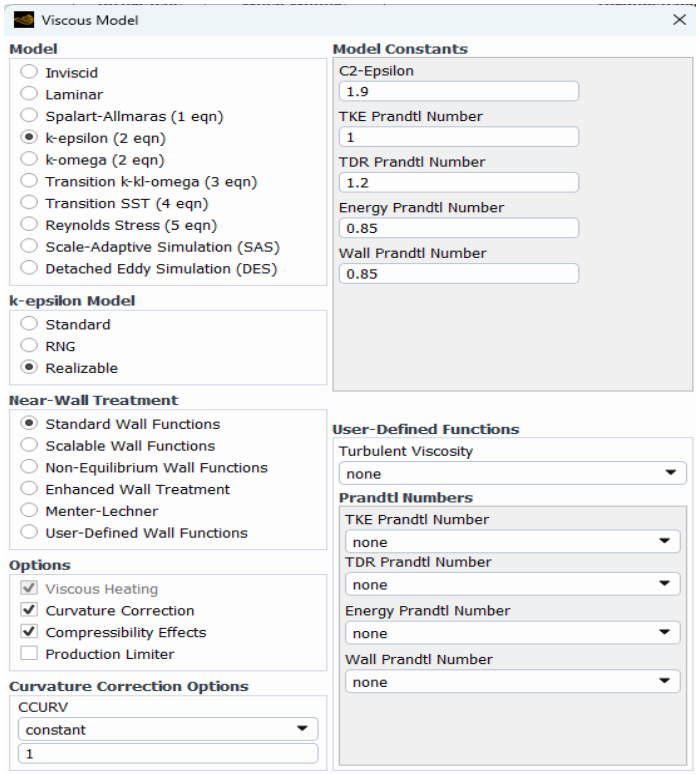

Figure 1 Viscous model settings

The energy equation is enabled and the k-epsilon (realizable) model is chosen for this simulation. For the material properties, the air is set as the fluid material and the density is of ideal gas with viscosity set to Sutherland three coefficient method. Specific heat is set as a constant value of 1006.43 J/kg K and the thermal conductivity value is 0.0242 W/(m k).

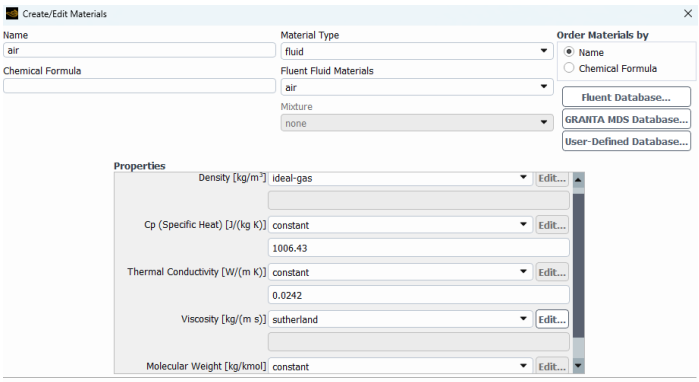

Figure 2. Material properties of Air

The boundary conditions were used for the flow and the inlet boundary is set as the pressure far-field and for the direction of the flow, both the x and y directions were assigned with parameters

to change them according to the angle of attack.

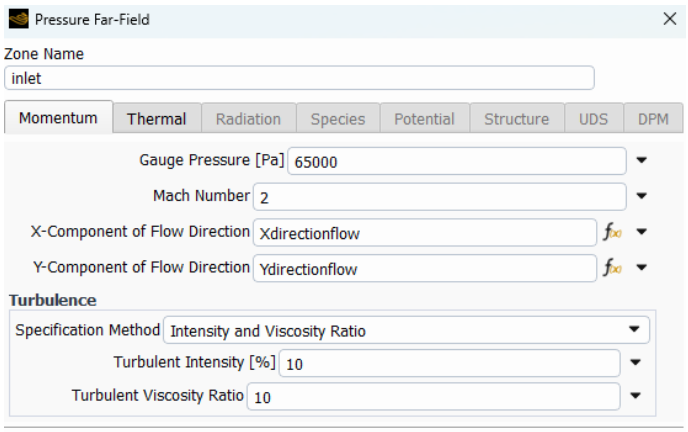

Figure 3. Boundary conditions

The Mach number of this flow is 2 at the initial position and the gauge pressure value is 65000 Pa. The temperature at these conditions is 254 K. The operating conditions are at zero pascals.

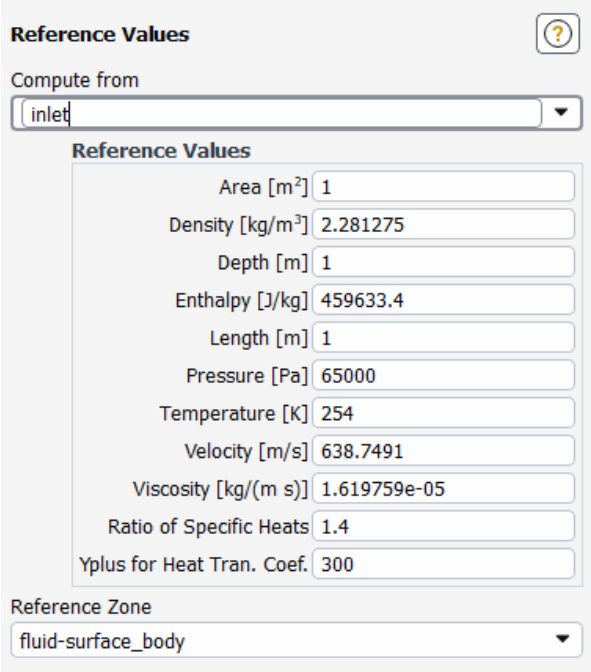

Figure 4. Reference values